Engineering the fracture resistance of 2H-transition metal dichalcogenides using vacancies: An *in-silico* investigation based on HRTEM images

Hoang Nguyen [a,†,#], Xu Zhang [a,†], Jianguo Wen [b], Xiang Zhang [c], Pulickel M. Ajayan [c], Horacio D. Espinosa [a,d,*]

[a] Theoretical and Applied Mechanics Program, Northwestern University, 2145 Sheridan Rd., Evanston, IL 60208, USA
[b] Center for Nanoscale Materials, Argonne National Laboratory, Lemont, IL 60439, USA
[c] Department of Materials Science and NanoEngineering, Rice University, 6100 Main Street, Houston, TX 77005, USA
[d] Department of Mechanical Engineering, Northwestern University, 2145 Sheridan Rd., Evanston, IL 60208, USA

Vacancy engineering of 2H-transition metal dichalcogenides (2H-TMDs) has recently attracted great attention due to its potential to fine-tune the phonon and opto-electric properties of these materials. From a mechanical perspective, this symmetry-breaking process typically reduces the overall crack resistance of the material and adversely affects its reliability. However, vacancies can trigger the formation of heterogeneous phases that synergistically improve fracture properties. In this study, using $MoSe_2$ as an example, we characterize the types and density of vacancies that can emerge under electron irradiation and quantify their effect on fracture. Molecular dynamic (MD) simulations, employing a re-parameterized Tersoff potential capable of accurately capturing bond dissociation and structural phase changes, reveal that isolated transition metal monovacancies or chalcogenide divacancies tend to arrest the crack tip and hence enhance the monolayer toughness. In contrast, isolated chalcogenide monovacancies do not significantly affect toughness. The investigation further reveals that selenium vacancy lines, formed by high electron dose rates, alter the crack propagating direction and lead to multiple crack kinking. Using atomic displacements and virial stresses together with a continuum mapping, displacement, strain, and stress fields are computed to extract mechanistic information, e.g., conditions for crack kinking and size effects in fracture events. The study also reveals the potential of specific defect patterns, "vacancy engineering," to improve the toughness of 2H-TMDs materials.

Keywords: Transition metal dichalcogenide; Vacancy engineering; Fracture energy; Phase transition; Crack kinking; Size effect; Atomistic-to-continuum mapping

Introduction

Since their discovery in 1923 [1], transition metal dichalcogenides (TMDs) have been considered a prime candidate for transistors in electronic devices, owing to the presence of a direct bandgap in their phonon structures [2–3]. This feature also enabled engineers to use TMDs as optical emitters and photodetectors [4]. In addition, their use in spintronics and energy harvesting is governed by strong coupling, either between their

* Corresponding author at: Theoretical and Applied Mechanics Program, Northwestern University, 2145 Sheridan Rd., Evanston, IL 60208, USA.
  E-mail address: Espinosa, H.D. (espinosa@northwestern.edu)
† These authors contributed equally.
# Current affiliation: School of Engineering, Brown University, 184 Hope St, Providence, RI 02912, USA

spin orbits [5] or between their crystalline structure and electrical polarization [6]. Even though a variety of TMDs stable phases have been observed at room temperature, in this study we focus solely on hexagonal TMDs (2H-TMDs). The methodology and findings, however, could be useful to other types of TMDs. 2H-TMDs, e.g., $MoSe_2$, possess a hexagonal ring structure, with Mo and two Se atoms at the lattice points, which preserves a 3-fold rotation symmetry when the viewpoint is along the c-axis. Introduction of vacancies can occur during multiple processes such as chemical vapor deposition (CVD) [7], exfoliation – if as-synthesize samples are in multilayered form [8], and electron irradiation [9–10], which can break the aforementioned symmetry and modify the fundamental properties of 2H-TMDs. For example, Truong et al. [11] showed that inversion-domain grain boundaries, on an $MoSe_2$ monolayer, acted as metallic one-dimensional chains that narrowed the phonon band gap when compared to the pristine counterpart. Interestingly, the formation of this boundary in $MoSe_2$ monolayers requires the presence of chalcogen vacancies [12]. In another example, C. Wei and co-workers showed that isolated chalcogen vacancies, generated via in-vacuo annealing, could enhance MoS_2 and WS_2 catalytic activity [13]. Likewise, a theoretical study [14] showed that vacancies in 2H-TMDs modified the shape of the conduction and valence band of these materials and hence decreased their electron mobility.

Beyond electrical, thermal, and catalytic properties, various opto-electronic responses in the presence of vacancies, were identified in 2H-TMDs. This opens an opportunity to fine-tune their properties by precise defect manipulation [15,16]. However, one aspect that has not been fully addressed is the impact of vacancies on the *mechanical* responses of 2H-TMDs. Point, line, and area vacancies have been shown to cause disruptions in mechanical fields and local stress concentration, which will adversely affect the integrity of the monolayers by reducing their critical strength [10,17,18]. In addition, they can significantly lower the service lifetime of a device even though the applied stress or strain is below the critical threshold needed to cause abrupt failure [19]. Alternatively, the stress concentration may trigger undesired changes in the atomic structure [20], which could lead to unexpected behavior of 2H-TMDs [21] and, more generally, other types of 2D phases [22,23]. Therefore, characterizing the impact of vacancies on the mechanical properties of 2H-TMDs monolayers is imperative. In 2016, Wang et al. performed a high-resolution transmission electron microscopy (HRTEM) characterization of crack propagation in monolayer MoS_2 and discovered a crack blunting effect arising from S vacancies [24]. Using molecular dynamics (MD) simulations, they predicted a non-monotonic trend of MoS_2 energy release rate when S vacancies increased in density and agglomerated into S vacancy lines. Another experimental effort by Falin et al. [25] used nanoindentation to investigate the effect of vacancies generated by exposure to air in WS_2, WSe_2, WTe_2 monolayers. Numerically, Mahata et al. [26] investigated the effect of vacancies on the ultimate strength and the Young's modulus of MoS_2 using atomistic simulations. A few other numerical and experimental reports can also be found elsewhere [27]. However, only recently, Huang et al. [28] and Zhang et al. [29] achieved precise manipulation of electron irradiation, in HRTEM, to drive the propagation of a

sharp crack while simultaneously acquiring atomic images. Using image analysis, Zhang et al. [29] computed strain fields, around the crack tip, and extracted quantitative data of crack toughness in *pristine* 2H-TMDs. These high-fidelity experimental data not only agreed with the bonding energy predicted by density function theory (DFT) but also revealed that nonlinearities, arising from bond dissociation, were confined to a small region ahead of the crack tip with a characteristic dimension of about 1 nm. Furthermore, the experimentally determined energy release rate and surface atomic structures, behind the crack tip, were predicted using an independently parameterized Tersoff force field.

To apply a similar experimental characterization to the fracture response of defective monolayers, one would need to first estimate the effect of vacancies on toughness and predict near-tip deformation and stress states to determine stable conditions for crack propagation. As Zhang et al. [29] indicated, in radiated in-situ TEM fracture experiments, the response of the monolayer is governed by its stiffness and the residual stress arising from sample adhesion to the substrate. Consequently, random creation of vacancies typically degrades the sample stiffness (see Fig. 2 of Zhang et al.'s paper [29]), which prevents crack extension. Therefore, achieving crack extension requires performing in-situ HRTEM experiments with load or displacement control setups, which are not only very challenging but would also require the creation of complex in-situ TEM methodologies and protocols. Furthermore, insights from atomistic modeling of the fracture processes as well as toughness estimates, using well-parameterized force fields, would be needed to advance a fundamental understanding of the role of vacancy types, density, and organization in the experimental design. Such understanding can provide a framework based on which, more complex experimentally observed vacancies, such as 4|4G boundaries [12] and $MoSe_6$ [30] vacancies can be analyzed.

In this study, we focus on the MD modeling of $MoSe_2$ as a model material system. To achieve accurate and reliable predictions of fracture response, we use the Tersoff potential, which as previously highlighted can capture complex atomic environments associated with the crack propagation processes, e.g., atomic bond dissociation in different coordination-number scenarios. A Tersoff potential, parameterized using a multiobjective optimization protocol [82], is employed due to its ability to capture the complexities mentioned above. Details are provided in section SI-2. We note that in contrast to the previous version [82], the set of parameters here identified are more weighted towards bond dissociation/formation in the large-deformation regime. Hence, this new set of parameters can capture energy landscapes and stress–strain behaviors, corresponding to both uniform and non-uniform bond dissociation pathways in pristine monolayers, as explained in a later section. We also note that the energy barrier of the 2H-1T phase transformation is described more accurately when compared with the barrier reported in Zhang et al. [82]. This is achieved without compromising near-equilibrium properties. Such a balance was obtained by focusing the training on data with the bond lengths and coordination numbers that are representative of atomic environments occurring during the fracture process, including their transition. This accuracy is manifested by matching not only

atomic bond evolution during separation (see Fig. 5 of Zhang et al.'s paper [29]), but also the strain mapping and the resulting critical J-integral values (see Fig. 5 of Zhang et al.).

Aiming at a realistic description of vacancy during MD simulations, we performed HRTEM imaging of $MoSe_2$ monolayers, when subjected to specific doses of electron irradiation. The density of vacancies was quantified for as-synthesize $MoSe_2$ monolayers, after transfer to a TEM grid using the protocol described in Dong et al. [31] and aberration-corrected HRTEM at a minimum dose rate of 10^{-6} e^- nm^{-2} s^{-1}. Next, tuning the e-beam irradiation to higher dose rates, up to 3×10^{-7} e^- nm^{-2} s^{-1}, we tracked the evolution of vacancies and quantified the number densities and spatial distributions of vacancies as a function of electron dose rate. Such spatiotemporal information was then correlated to the formation energies of each vacancy type to explain their formation probability. After choosing a dose rate (using a rationale to be presented later) we predicted the effect of vacancies on the mechanical behavior of $MoSe_2$. These predictions aimed to (1) differentiate the role of each fundamental vacancy type in altering fracture behavior, and (2) estimate the statistics of the effect of vacancy type on fracture toughness, including their mean and standard deviation. As such, this study is expected to guide the defect engineering step and experimental designs focusing on vacancy type, density, spatial distribution, and their combination thereof.

To gain insight into atomic mechanisms, analyses of crack-vacancy interactions were performed for each vacancy type. Furthermore, analyses were carried out employing atomistic-to-continuum mapping of stress, strain, and displacement fields [29]. These analyses include the calculation of the critical J-integral [32] to quantify changes in fracture energy, caused by each vacancy type, as compared to the pristine material critical J-integral [29]. Another analysis used the crack kinking theory to determine the governing law for crack propagation direction. Lastly, by employing the size effect method presented in [33], we estimated the size of the inelastic zone and its dependence on defect type. The in-silico investigation concludes with (1) a summary of the role of vacancies in preventing abrupt and premature failure of 2H-TMDs, and (2) suggested strategies for vacancy-

engineering aiming to improve $MoSe_2$ monolayers' resistance against fracture.

Molecular dynamics simulations to predict the effect of vacancies on fracture

As mentioned earlier, we carried out MD simulations, with the high-fidelity Tersoff potential (denoted as Tersoff-MoSe-7.0 in this study), to examine atomic behaviors at the crack tip and edges when the crack interacts with specific vacancy types. The high fidelity of the interatomic potential was previously demonstrated by us [29,82] for *pristine* $MoSe_2$. We accomplish this not only by matching MD and DFT results, for a large set of material properties (SI-Fig. S5-6), but also by comparing toughness and crack surface atomic structures, to numerical predictions [29].

It is known that in materials with covalent bonds, high stress concentration leads to a cascade of bond breakage events. Fracture mechanics also reveals that crack propagation can be altered through suitable changes, e.g., via the specific arrangement of vacancies [34] in the crack front. However, what vacancy type, density, and organization is most effective in toughening remains unknown. This motivated us to pursue an in-depth study of vacancy type, density, and pattern using *in-silico* predictions. To accomplish this, we performed MD simulations on an 80×40 nm rectangular domain containing a 20-nm long crack (see Fig. 1). The monolayers were loaded along the y direction, and the boundary conditions were set to be free at the left and right edges, with periodicity at the top and bottom edges. For the loading, we applied a fixed loading rate up to a point close to failure and then reduced it to a lower value to avoid excessive kinetic energy in bond breakage, when the energy stored in the strained monolayer was released abruptly (see the Methods section for more details). Theoretically, the crack would propagate at a very high speed; however, due to the intrinsic viscosity of the applied thermostat [35], the propagating crack was captured in a sequence of atomic snapshots. The atomic positions at these snapshots were used in an atomistic-to-continuum mapping scheme (see the Methods section), which was then used to compute the critical J-integral [32,36]. To achieve statistically meaningful results, multiple contours were used to compute this integral.
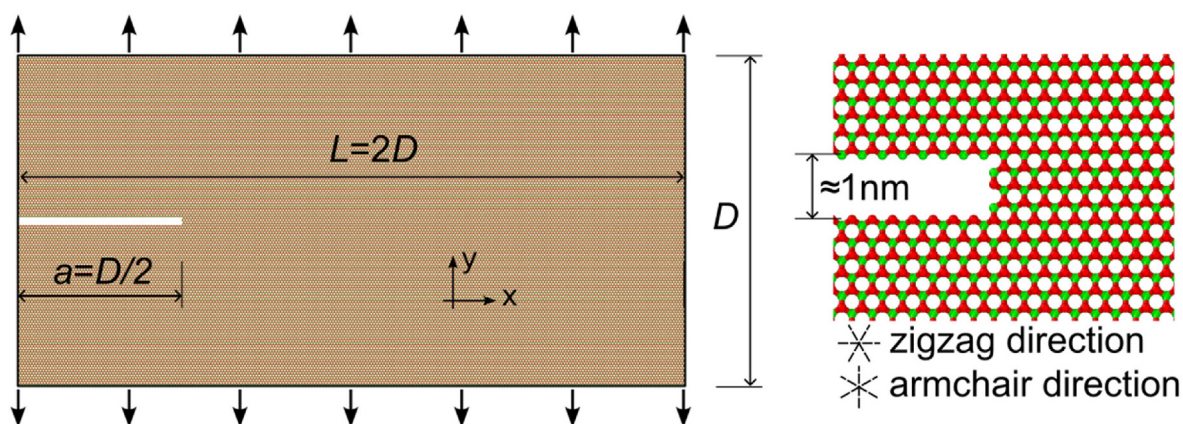

FIG. 1

Configuration used in $MoSe_2$ fracture simulations (D = 40 nm, x-axis aligned with the zigzag direction). Details of notch width and tip in the initial configuration.

Results and discussions

Characterization of vacancies generated by electron irradiation

It is known that by tuning the electron beam in the TEM, the electron-material interaction can be used to gradually elevate the density of vacancies, with various possible vacancy types, while retaining the integrity of the entire monolayer. It is also known that atomic vacancies in 2D monolayers inevitable form during the CVD-growth and transfer processes, yet their densities are relatively modest [9,31]). To investigate the controlled formation of vacancies, we performed experiments at various electron dose rates (with unit e-nm^{-2}-s^{-1}) while keeping the total dose per unit area constant (1.43×10^8 e-nm^{-2}, note that this was lower than the one used by Zhang et al. [9]). Using HRTEM imaging, at a very low dose rate of 5.8×10^5 e-nm^{-2}-s^{-1}, we detected the existence of isolated Se (iSe), isolated Se$_2$ (iSe$_2$), and isolated Mo (iMo) vacancies (Fig. 2). To achieve accurate quantification of these vacancies, we used several defocus values (Δf) and settled at the range of [−1;1] nm, within which the Mo and Se atoms were distinguishable (see Figs. 2a, S11-12 and Methods section). The sites of vacancies are identified from lattice points with lower intensity peak. While the iMo are distinguished from iSe/iSe$_2$ vacancies based on their relative atomic positions within a hexagonal ring, the iSe$_2$ vacancies show no well-defined peak compared with iSe, which is represented by a distinctive peak having intensity lower than the lattice points with two Se atoms. In Fig. 2a, we depict two 2 representative images containing iSe, iSe$_2$ and iMo, labeled by green, yellow, and blue circles, respec-

tively. At each dose rate, we characterized the density of all vacancy types and averaged them based on 23 regions (2×2 nm each) within an HRTEM image. As shown in Fig. 2b, the densities of iSe, iSe$_2$, and iMo vacancies in MoSe$_2$, visualized at 5.8×10^5 e-nm^{-2}-s^{-1}, are estimated to be 0.207, 0.042, and 0.004 nm^{-2}, respectively. At these densities, there are several regions in which the MoSe$_2$ monolayers look "pristine" as shown by Zhang et al. [9,29]. As expected, the emergence of these vacancies is not equally probable but inversely correlated with their formation energy, i.e., 1.143, 2.159 and 2.259 eV-nm^{-2}. Note that these values are larger than the normalized kinetic energy of an atom at room temperature (0.176 eV-nm^{-2}), which implies that the formation of additional vacancies could not occur spontaneously between the flake transfer and the low dose imaging [29,31]. Therefore, the total vacancy densities reflect those generated during fabrication and monolayer transfer (background vacancy density), and those arising from the electron-material interaction. Indeed, it is known that electron irradiation generates knock-on damage by transferring kinetic energy to the atoms in the target materials, inducing displacement and atomic oscillations [16]. In addition, the electron irradiation is responsible for both ionization damage and electronic excitation in the monolayers [37], which decreases the knock-on threshold energy of the target atoms [28].

Even when the formation energy difference between iMo and iSe$_2$ vacancies is not significant, the formation probability of the former type is one order of magnitude smaller than the latter. We
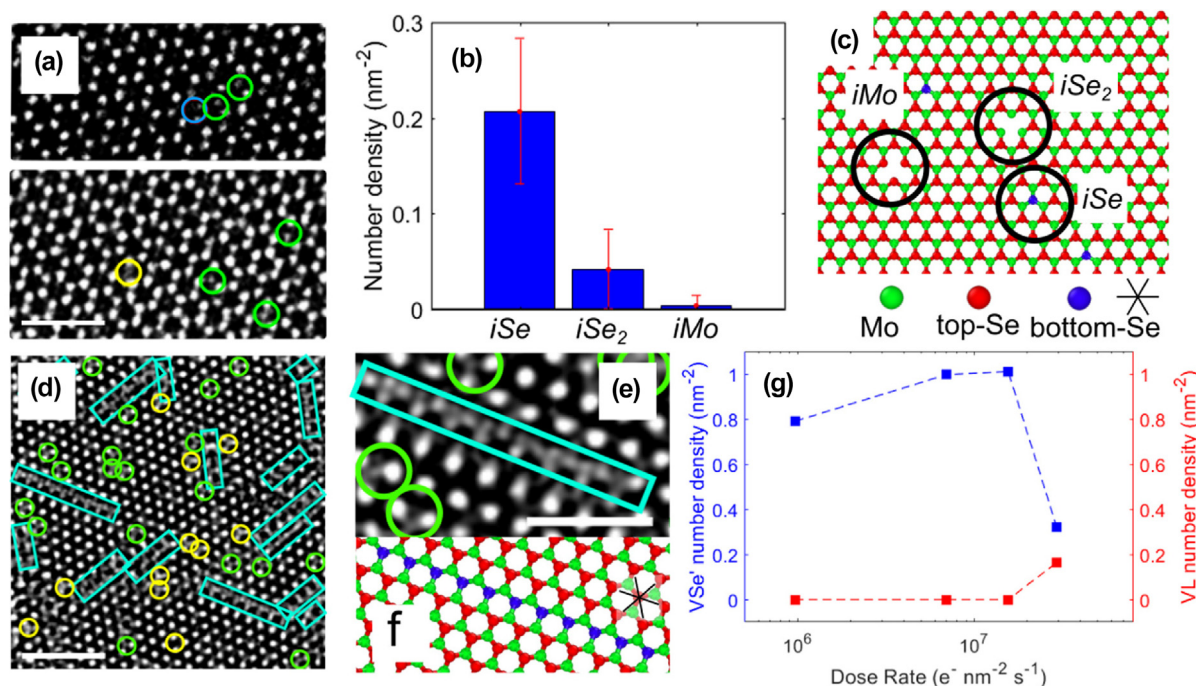

FIG. 2

(a) High-resolution transmission electron microscopy (HRTEM) characterization of a suspended MoSe$_2$ monolayer deposited on a holey Si$_3$N$_4$ TEM grid at an imaging dose rate of 5.8×10^5 e-nm^{-2}-s^{-1}. The isolated Se (iSe) vacancies, isolated Se di-vacancies (iSe$_2$) and isolated Mo (iMo) vacancies are marked by green, yellow, and blue circles, respectively; (b) The corresponding vacancy densities in a), measured from 23 regions of 2×2 nm in an HRTEM image, and (c) their atomic representation. (d-e) HRTEM images depicting the emergence of Se vacancy lines at a dose rate > 1.5×10^7 e-nm^{-2}-s^{-1}, and f) atomic representation of a vacancy line sharing the same characteristic length and orientation as in e). (g) The evolution of iSe vacancies and vacancy lines as a function of electron dose rate. The total dose was kept constant for the four conditions at 1.43×10^8 e-nm^{-2}. Scale bar: (a) 1 nm, (d) 2 nm, (e) 1 nm.

attribute this to the nature of the TMD structures. The Mo atomic layer is sandwiched by two Se atomic layers; electrons need to disturb the Se orbitals before interacting with the Mo atoms. Indeed, after overcoming the loss of energy via phonon-electron and electron–electron inelastic scattering, if the remaining energy of the electron is still adequate to knock out the Mo atoms and if the electron is not diffracted, such a vacancy can be created.

We observed that when the dose rate increases, the density of all vacancies also increases while the ratios of different types remain approximately constant. Between 1.5×10^7 e-nm^{-2}-s^{-1} and 2.93×10^7 e-nm^{-2}-s^{-1}, the fourth type of vacancy, Se vacancy lines (marked as cyan rectangles in Fig. 2d-e), started to form. The characteristic size of these lines was approximately 1 to 1.4 nm. After confirming the presence of lSe at the defocus range mentioned above, we also observed that when the defocus value in Fig. 2d was varied within the range of [−10; −5] nm, Mo atoms and lSe were more visible, facilitating the characterization of this type of vacancy. Fig. 2g shows the density of all vacancy types when the dose rate is varied between 5.8×10^5 e-nm^{-2}-s^{-1} and $\sim 1.5 \times 10^7$ e-nm^{-2}-s^{-1}. At a dose rate of approximately 0.7×10^7 e-nm^{-2}-s^{-1}, the total density of Se vacancies rose to 1 nm^{-2}. Moreover, higher dose rates resulted in an increase of Se vacancy line density and a decrease of the density of isolated Se vacancies, which suggested a synergy between these two types. Indeed, when the electron irradiation supplied enough energy, the Se atoms near the isolated vacancies hopped over the energy barrier of ionic migration and started to assemble into vacancy lines, which represented a minimum energetic state [38]. We also observed that a significant number of vacancy islands would nucleate, if the dose rate were to be increased beyond 2.93×10^7 e-nm^{-2}-s^{-1} or kept constant for more than 10 seconds [9], ultimately leading to failure of the MoSe$_2$ monolayer.

From our HRTEM observations and literature reports, the following conclusions can be made. First, the fundamental types of vacancies were of 0 or 1 dimension. Other vacancies, e.g., MoSe$_6$, can be generated by agglomeration of these fundamental types under electron [9] or focused ion beam with a more aggressive irradiating condition. Second, the spatial distribution of vacancies was stochastic due to the random bombardment of electrons within the observing window. This makes an experimentally controlled crack propagation through a pre-defined defective region (with electron beam irradiation) more challenging, calling for a careful experimental design based on numerical predictions. Finally, other indirect methods might generate less pervasive damage [38–39]; however, such methods generate similar vacancy types, based on the superposition of the fundamental ones here described, so fracture responses for other vacancy types can be inferred from this study. Consequently, in subsequent sections, we used atomistic simulations to provide in-depth knowledge of how these fundamental vacancy types, *with densities estimated from HRTEM quantification*, interact with the tip of a crack. Specifically, Fig. 2c and f depict vacancy representations used in the simulations. The accuracy of the simulations hinge on the accuracy of the interatomic potential to replicate *ab initio* training data in the large deformation regime, which has important implications on the MoSe$_2$ mechanical response in the presence of vacancies and cracks. Therefore, we performed parametrization using an *unprecedented* number of properties as well as validations against both ab-initio *and* experimental data obtained on MoSe$_2$ monolayers (see section SI-2 and another study from the authors [29], respectively).

Toughness and crack tip features in pristine and vacancy containing atomic structures

We begin by summarizing a few results on "pristine" MoSe$_2$, a baseline for comparison. A snapshot of the crack tip and crack edges, on a pristine monolayer, when the crack propagated to half of the domain size, is shown in Fig. 3a. Along the crack, edges with single Se atoms and distorted hexagonal rings are observed in the simulations. This feature is consistent with experimental observations (see Fig. 3a and Zhang et al.'s paper [29]). We note that these types of edge structures could not be formed by the mere removal of atoms, but only through a stress-assisted dissociating process (Fig. 3b). Another observation is that in MD simulations and experiments, the rate of energy release is much faster than in DFT simulations, which can be attributed to differences in the simulated domain size (80×40 nm^2 in MD and 2×2 nm^2 in DFT). [34] This results in a more abrupt transition (Fig. 3c), in the MD and experimental cases, even though reactants and products correspond to the same transition process. This stemmed from the fact that the characteristic length resulting from bond dissociation is approximately 6–8 Å ($\sim 2 \times$ Mo-Se bond length and on the same order of the DFT simulation domain), while in the much larger MD and experimental domains, the rate of energy release during bond dissociation is not large enough to prevent a snap-back instability [34].

The crack tip depicted in Fig. 3a also exhibited several features resembling those observed in atomic configurations revealed by HRTEM and DFT [29], such as rotation of the Se-Mo-Se angular structure and stretching of the bonds at the crack tip (see Fig. 3-a-b and Fig. 1 of Zhang et al.'s paper [29]). The excellent agreement, in both atomic surface reconstruction along the crack edges and the nonlinear fracture energy J_c between experiments and predictions based on the ab-initio-informed potential [29], provides the needed confidence on the predictive capabilities of the methodology. In turn, this enables investigation and reliable quantification of toughness and atomic mechanisms of crack-vacancies interaction. Consistent with the HRTEM observation of vacancy type and densities, we investigated the four observed vacancy types. We employed a density of 0.207 nm^{-2} for iSe, iSe$_2$ and iMo, For the case of lSe, we used a density of 0.188 nm^{-2}. Note that such density corresponds to the limit measured experimentally before monolayer disintegration at higher electron dose rates.

The qualitative and quantitative effects of these four vacancy types are summarized in Fig. 3d-g. If iSe vacancies are present in the vicinity of a crack tip (Fig. 3d and Movie 1), they mildly deflect the crack path but do not significantly alter the fracture resistance. The prediction is consistent with the experimental J_c reported in Zhang et al.'s paper. [29] Indeed, the experimental toughness of MoSe$_2$ monolayers, which inevitably contained mainly iSe vacancies, although with a density likely lower than the one used in this study due to the low imaging dose used by Zhang et al. [29], is lower than the MD result for the "pristine"
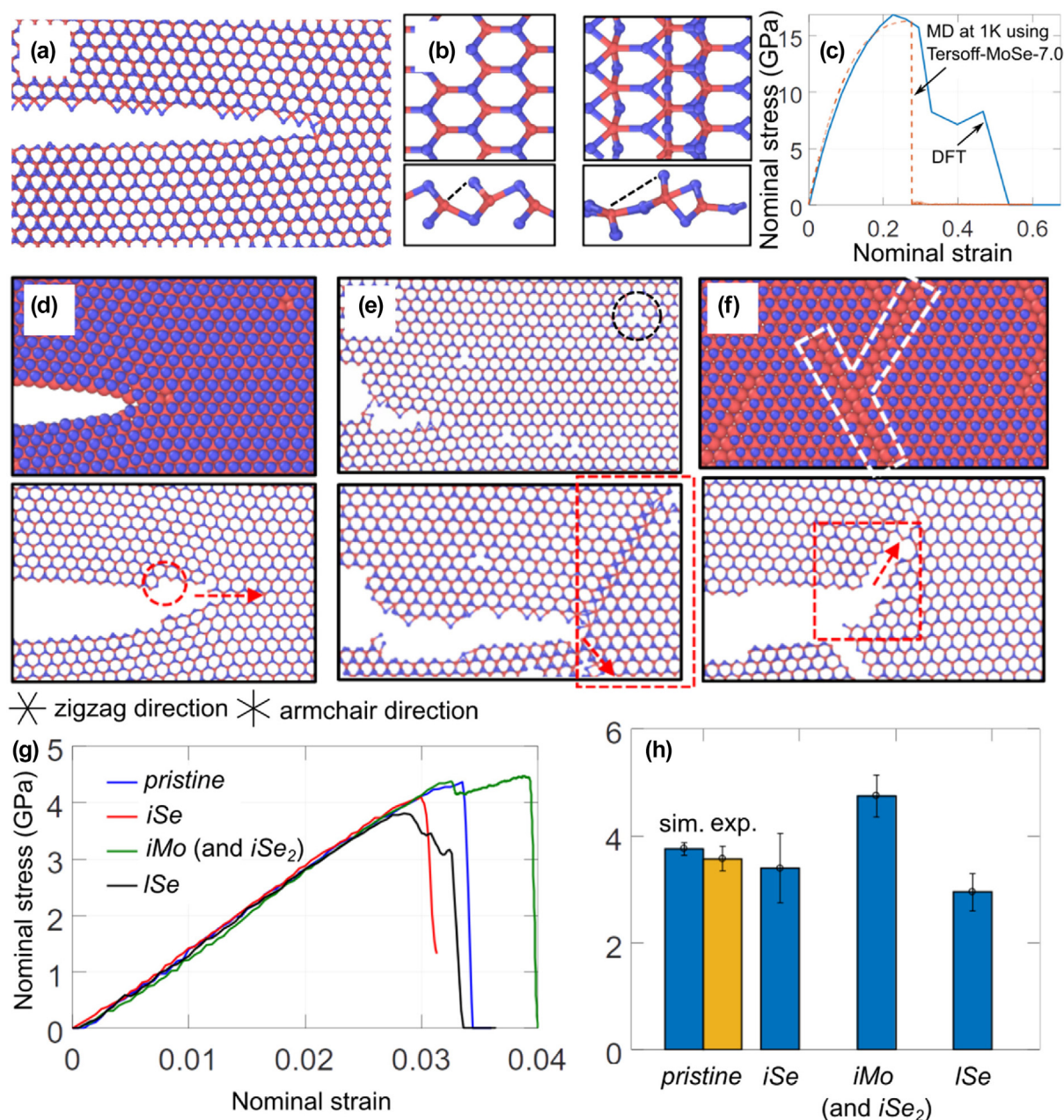
FIG. 3

(a) Crack tip and crack edges on a pristine monolayer in the aftermath of the bond dissociation, as represented in b), and found in HRTEM images [29]; c) Note that MD at 1°K shows a faster drop in nominal stress after bond dissociation; (d-f) Atomic images depicting the interaction between the main crack and *iSe*, *iMo/iSe2*, or *lSe* (red arrows show the direction of crack propagation); (g) Typical nominal stress–strain curves for the domain containing a crack and various atomic structures; and (h) The effect of vacancy type on MoSe2 fracture energy including standard deviation (yellow bar indicates the experimental value as reported in Zhang *et al.*'s paper [29]).

MoSe2 but slightly higher than the MD result for *iSe* (Fig. 3h). Other types of defects, on the contrary, had a more notable impact on the fracture response and the corresponding fracture energy.

Due to the similar effects on fracture produced by *iMo* and *iSe2*, their atomic behaviors are shown together in Fig. 3e. When vacancies of these types are present in the near-tip area, they blunt the tip with a local structure similar to a 4|4P [15] (we called such a structure 4|4P-like) and locally decrease the stress singularity. The nucleation of such a structure triggers an edge-

nucleated slip motion in the ±60° directions (Fig. 3e and Movie 2). This is enabled by the tip shear stress at ±60° and the presence of another isolated vacancy along the slip plane. The deformation process lowers the associated energy and stress barriers, allowing Se atoms to hop to a nearby location and initiate a slip motion. At the same time, the interruption of part of the 4|4P-like structure and the decrease in stress singularity (due to the bluntness of the crack) increases the energy barrier for straight crack propagation (as shown in a later subsection). As this barrier becomes larger than the one needed for slip, the 4|4P-like bound-

ary traps the propagating crack. As a result, the crack propagates along a different path, which requires an increase in driving force and a higher fracture energy. By performing simulations on multiple replicas, we found that the probability of these events is about 20% when vacancies are distributed randomly. This percentage implies that the probability of observing such an event experimentally would be relatively low even though the fracture energy increase is significant when the crack tip is trapped. The average J_c, obtained by simulating several different replicas, is reported in Fig. 3g.

The presence of Se vacancy lines, around the crack tip, also impacts the fracture behavior of MoSe$_2$ monolayers. Such vacancies tend to deflect the crack towards the vacancy line direction, resulting in a tortuous crack path (Fig. 3f and Movie 3). In some cases, when two vacancy lines intersect, extra free edges are created, leading to a higher dissipated energy. The crack tortuosity results in a more gradual release of energy. However, due to the loss of one layer of Se atoms and the brittle nature of covalent bonds, the strength and overall fracture energy decreases when compared to pristine MoSe$_2$ (see Fig. 3g). It is worth noting that, compared with the "pristine" monolayers, the standard deviations of the critical J-integral values, for the defective monolayers, are larger on account of the random distribution of vacancies (at the same density).

Interestingly, the fracture behavior in the presence of vacancies brought up two contrasting behaviors. In the presence of iMo and iSe$_2$ vacancies, crack propagation occurred in the direction opposite to the direction of the vacancies. In other words, vacancies repelled the crack. On the contrary, Se vacancy lines attracted and guided the crack along their orientations. Therefore, the interplay between these types of defects opens a vast design space for defect engineering towards increasing the material resistance against fracture, a much-needed feature to increase the reliability of nanodevices and sensors based on 2H-TMDs. It is worth highlighting that from the HRTEM quantifications, the dose rate and probabilities of the various vacancy types make their controlled engineering challenging. However, Fig. 2d provides evidence that a mixture of vacancy types is experimentally possible.

Crack path selection in the case of iMo/iSe$_2$ vacancies – Energetics and driving forces
While the effect of Se vacancy lines was easily understood because the energy consumed to break one layer of Mo-Se bonds was lower than that for two layers, the mechanism behind the strengthening effect caused by iMo/iSe$_2$ vacancies is less obvious. When the crack encounters an iMo or iSe$_2$ vacancy, a deformation process involving a slip motion at $60°$ (zigzag direction) becomes possible (Fig. 4a and Movie S1). The motion brings two Se atoms closer to the center of the adjacent hexagonal ring, potentially leading to the formation of a locally stronger structure (4|4P-like). A second possibility is crack extension by the propagation of bond breakage in the direction of the main crack (mode I, Fig. 4b and Movie S2). A third possibility is crack propagation in the $-60°$ (another zigzag direction) (Fig. 4c and Movie S3). To determine which path is energetically favorable, we used the nudged elastic band (NEB) method, [40,41] and computed the energy barrier for the three possible crack tip propagation

scenarios (Fig. 4d). The energy landscapes revealed that distortion of the atomic structures in shear, due to the presence of vacancies in the slip direction at $60°$, presents the lowest energy barrier making such deformation process the most likely to occur. The energy barrier corresponding to straight crack propagation, is the highest, due to interruption of part of the 4|4P-like structure and the presence of an isolated vacancy ahead of the tip that decreases stress concentration. Therefore, it is obvious that the structural change caused by the migration of Se atoms along the slip direction traps the crack temporarily. Upon crack trapping, the crack is most likely to propagate along a path at $-60°$ (Fig. 4c and Movie S3), which presents the second lower energy barrier (Fig. 4d). This explained the transition observed in Fig. 3d and the associated increase in fracture energy. We also note that after some crack extension, the crack propagation continues along the $0°$ direction (Fig. 4e).

Analyses of stress/strain/displacement fields based on atomistic-to-continuum mapping

Besides energetics, a mechanical analysis of the observed phenomena is necessary for extracting conditions for crack kinking and size effects in fracture events. To accomplish this, we map atomic stress, strain, and displacement fields, to the continuum counterparts using the scheme summarized in the Methods section. Continuum fields reveal the effect of vacancies on the spatial distribution of mechanical quantities (potential energy, displacement, stress and strain fields). We highlight similarities and differences between the cases using the equivalent (von Mises) stress and potential energy. For completeness, the color maps of other fields are provided in section SI-2. In all plots, a white-filled area represents the initial notch.

On a pristine monolayer, the Mises stress and its distribution along the x-direction [29] revealed that the size of the cohesive zone in pristine materials is approximately 0.8 nm. This zone is caused by the gradual force-energy release of the bond-dissociation process presented in Fig. 3b. Fig. 5a-b also confirm the presence of this cohesive length in the pristine monolayer. Fig. 5a depicts a zone with non-zero stress between the crack tip and the completely separated bonds. Similarly, in Fig. 5b, the loss of potential energy of the completely separated bonds (critical separation) is higher than the ones within the cohesive zone. The mapping of mechanical fields in the case of monolayers with iSe vacancies showed similar characteristics with the pristine monolayers (Fig. 5c-d), except for the ε_{yy}- and ε_{xy}-fields (see SI-Fig. S3) where the vacancies weakened the atomic structures surrounding them. This weakening effect leads to local bursts in the strain fields at the location of vacancies, yet it did not significantly change the fracture energy due to the scatteredness of vacancies.

Unlike other cases, isolated Mo vacancies resulted in the most significant mechanical field changes. For example, the stress fields showed the emergence of two areas with stress concentration, one of which is at the crack tip, and another is located at the end of the slip-line boundary where the iMo is located. The slip-line (4|4P-like) structure is stiffer than the usual hexagonal-ring structure of 2H-MoSe$_2$ and generates a stress concentration at the connecting region of the two structures (Fig. 5g-h). The
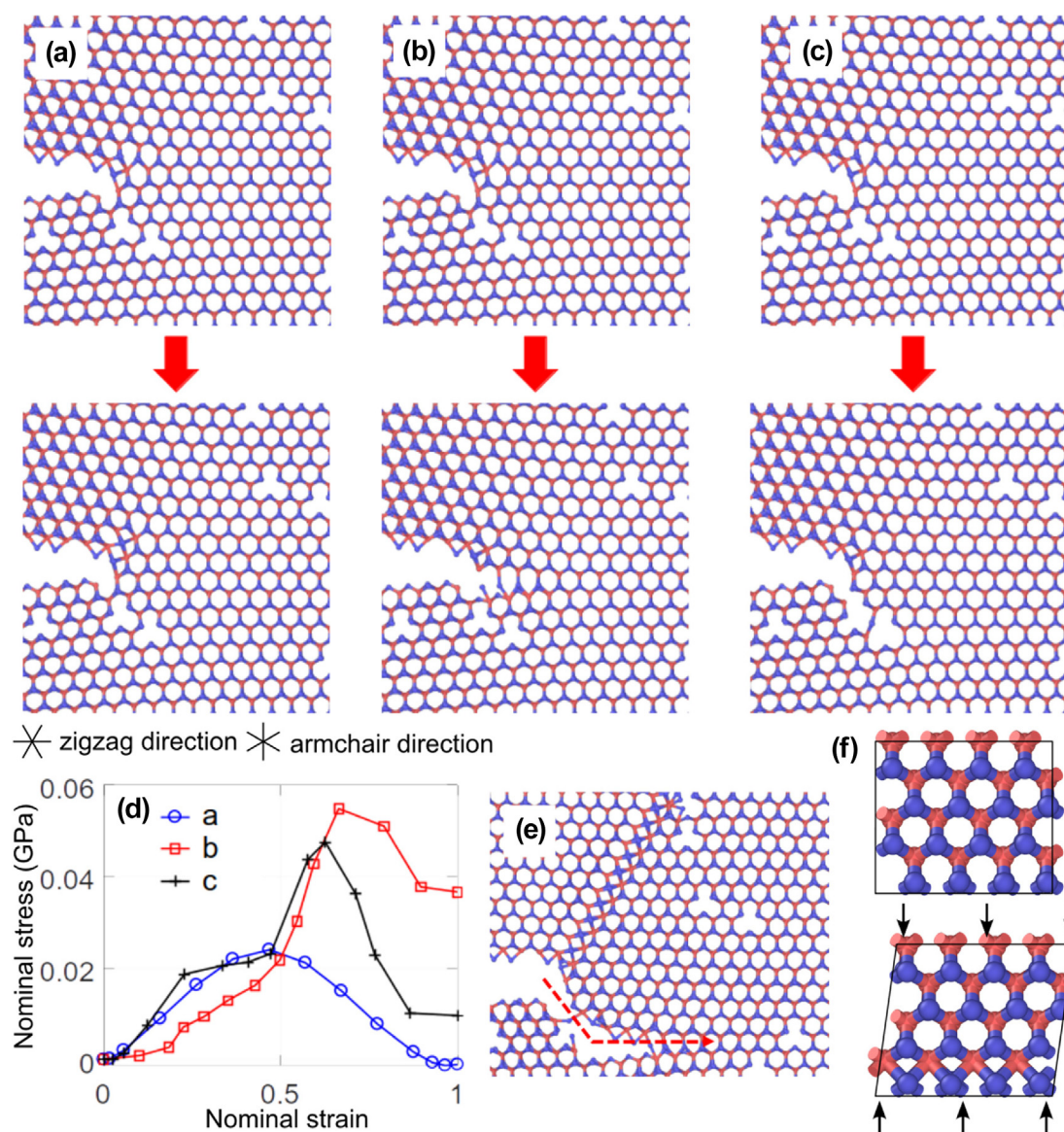
RESEARCH: Original Research

FIG. 4

(a-c) Three possible deforming process ahead of the crack tip, shearing along 60°, straight crack propagation at 0°, and crack extension at −60°, respectively; (d) Comparison of energy barriers between the three scenarios; (e) The shearing configuration and subsequent propagation of the crack after lattice trapping; and (f) Shear deformation-triggered formation of 4|4P-like structure, and relaxed structure after energy minimization.

strain distribution followed the same pattern, in which the shear strain shows an increase at two sides of the slip-line structure (SI-Fig. S4). However, unlike the shear strain distribution ahead of the tip, the distribution across the slip-line structure was parallel to such structure. This shows the difference between a slip displacement, like the case of dislocation glide, and the one resulting from an opening displacement (SI-Fig. S4). This inhomogeneous structure also causes a discontinuity within displacement fields (SI-Fig. S4), resulting in a distinctive strain value within this region. However, the distinctiveness in the shear is more significant than the normal component, which indicates that even though this slip-line structure enhances both shear and tensile modulus, the major deformation along 60° direction is sliding instead of separation. Note that the potential energy of this structure is higher than the one in the 2H phase (Fig. 4f).

Indeed, higher shear stresses and surrounding point vacancies are necessary to lower the energy barrier and equilibrium energy of this phase (stress-assisted transformation). Therefore, when the crack passes through this region, stresses are released, and the work supplied to form such boundary diminished making the phase reversible.

Significant differences in Mises stress and other mechanical fields also appear in the case of vacancy lines. Specifically, Fig. 5e illustrates a rotation of the tip stress field along an orientation of 60°. This is owing to the smaller modulus of the local vacancy-line structure, causing a stress release in the direction of propagation. The potential energy (Fig. 5f) also reflects this feature, in which the separation of bonds occurs along the 60° direction. We note that, even though the mapping of shear stress and strain shows similar features, the crack propagates in mode I
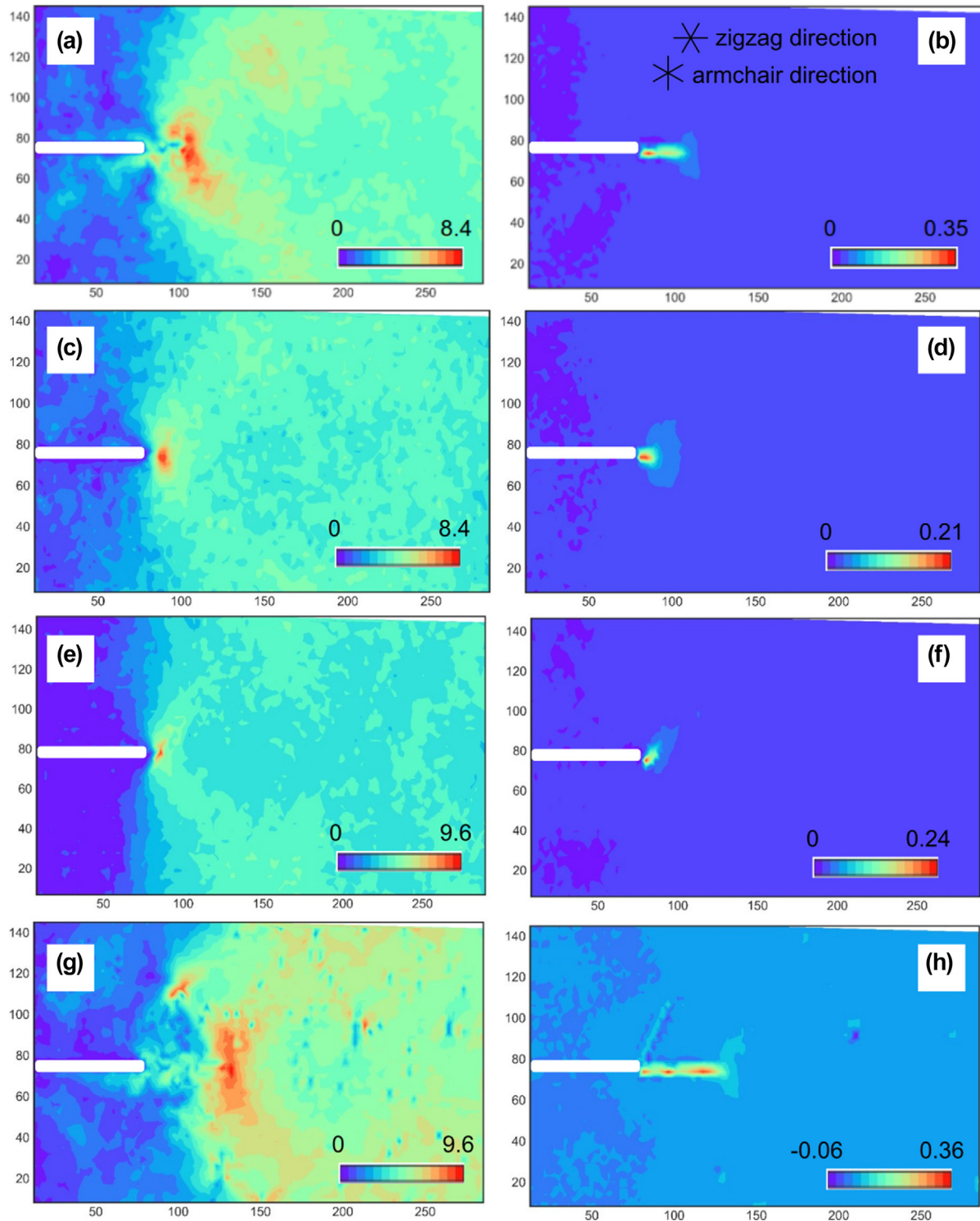
FIG. 5

Von mises stress distribution, σ_{Mises} (unit: GPa), and potential energy Π (unit: eV) for pristine monolayer (a-b) and monolayers with iSe (c-d), iMo/iSe$_2$ (e-f), and lSe (g-h) vacancies. Note that only a window of 15×30 nm^2 is shown.

as the burst in shear strain is smaller in amplitude compared with the burst in normal strain (a more rigorous argument will be presented in the next section). In addition, the shear stress field is less disturbed than the normal stress field (SI-Fig. S3). One noteworthy feature of the deformation fields is the discontinuity of the strain values across the vacancy lines.

Critical crack kinking angle based on the maximum tangential stress criterion

Even though the deflection of the crack path was rationalized using *posterior* MD atomic configurations and energy barrier analyses for different likely events, an *a priori* criterion to determine the angle at which a crack would deflect can be postulated based

on continuum fields, obtained from atomistic mapping, and a crack-kinking criterion. There are several such criteria for both isotropic and anisotropic materials, e.g., the maximum tangential stress (MTS) criterion [42], the maximum energy release rate criterion (MERR) [43], the minimum strain energy density criterion (SED) [44], and others [45,46]. Richard et al. [47] showed that the MTS criterion is sufficient to describe crack kinking behavior of brittle and quasi-brittle materials; hence, we here adopt such a criterion.

For anisotropic materials, the general form of this criterion can be written as [48]:

$$\sigma_\theta(\theta_0) + T(\theta_0) = \sigma_c(\theta_0)$$
$$\left.\frac{\partial}{\partial\theta}\left(\frac{\sigma_\theta+T}{\sigma_c}\right)\right|_{\theta_0} = 0 \tag{1}$$
$$\left.\frac{\partial^2}{\partial\theta^2}\left(\frac{\sigma_\theta+T}{\sigma_c}\right)\right|_{\theta_0} < 0$$

where $\sigma_\theta = K_I(\theta)/\sqrt{2\pi r_c}$, $\sigma_c = K_{Ic}(\theta)/\sqrt{2\pi r_c}$ are the tangential stress and its critical value for each direction, r_c is the length scale representing the fracture process zone size [33,49] (this size is taken to be 0.8 nm in this study based on the results presented earlier), K_I is the stress intensity function (its relation with J can be found elsewhere [33]), and T is the crack-parallel stress computed at r_c. These functions can be found in section SI-2.

We further enrich this theory by adding the angular dependence of the tangential strength, σ_c. Due to the intrinsic anisotropy of the MoSe$_2$ membrane, one can write σ_c as a function of the angle with respect to the x-axis (the zigzag direction):

$$\sigma_c = \sigma_{c,AC}\left[\mu_p + s_p cos(6\theta - \pi)\right] \tag{2}$$

where $\sigma_{c,AC}$ = 13.43 GPa is the tangential strength when the crack propagates in the armchair direction. μ_p, s_p are tuned such that the minimum tangential strength matched the fracture strength in the zigzag direction $\sigma_{c,ZZ}$ = 9.94 GPa. The value for intermediate angles between these two orientations are interpolated based on a cosine function. It is also obvious from this formulation that the tangential strength has a periodicity of π/3 (see Fig. 6).

In the presence of a slip-line boundary or a Se vacancy line, the directional effect arises at 0°, ±60°, ±120° (here 60° is chosen without loss of generality). Therefore, the change in tangential

strength is obtained by adding additional angular dependent terms, namely,

$$\sigma_c = \sigma_{c,AC}\left[\mu_p + s_p cos(6\theta - \pi)\right]$$
$$\pm a_s\Delta\sigma_{c,\pi/3}/\sqrt{[a_s cos(\theta - \pi/3)]^2 + [sin(\theta - \pi/3)]^2}$$
$$\pm a_s\Delta\sigma_{c,2\pi/3}/\sqrt{[a_s cos(\theta - 2\pi/3)]^2 + [sin(\theta - 2\pi/3)]^2}$$
$$\pm a_s\Delta\sigma_{c,0}/\sqrt{[a_s cos(\theta)]^2 + [sin(\theta)]^2} \tag{3}$$

The slip-line boundaries and Se-line vacancies can either enhance or weaken the fracture resistance of the pristine material when they appear at the crack tip. Hence, these modifications are reflected by the +/− Δσ$_c$ terms (positive for enhancement, negative for weakening). By performing MD simulations, the fracture energy of the mode I crack in the zigzag direction, armchair direction, slip-line boundaries, and Se-line vacancies are computed, assuming proportionality to the area under the nominal stress–strain curves (Fig. 3g) (see Table 1).

Predictions from the MTS criterion (Eq. (1) are given in Table 2. The criterion predicts that in the presence of the strengthening slip-line boundaries orienting at +60°, the angle for crack propagation is predicted to be −58°. By contrast, for the Se-line vacancy, the predicted angle is +60°.

Size effects as a method to determine the fracture process zone
From the previous results (especially the cases of *iMo* and *lSe*), it is clear that only vacancies located within a near-tip zone interact with the crack and alter the monolayer fracture behavior. Vacancies located outside of this zone would only affect the elastic modulus of the monolayer. Therefore, from an experimental design perspective, it is necessary to determine the size of such zone to properly investigate the effect of vacancies. The effect of vacancy density identified through HRTEM experiments, also provides guidance to preserve the stiffness of the specimen to avoid its degradation due to the excessive damage.

From Fig. 5, one can postulate that the inelasticity caused by inhomogeneities (i.e., the slip-line boundaries or Se-vacancy lines) can be lumped into one zone, usually referred to as fracture process zone or FPZ. Because inelastic deformations can form in
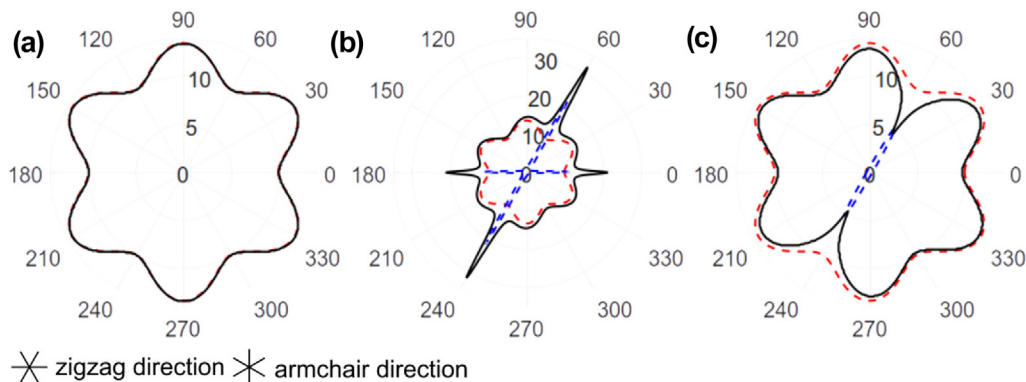

FIG. 6

Angular dependence of the critical strength σ_c of (a) pristine MoSe$_2$, (b) MoSe$_2$ with 4|4P-like boundary at 60°, and (c) MoSe$_2$ with a vacancy line at 60°. The stress unit along the radial grid is GPa. The data is plotted based on Eq. (10) and the parameters listed in Table 1.

TABLE 1

The values of parameters identified from MD simulations.

Quantity	$\sigma_{c,AC}$(GPa)	μ_p	s_p	a_s	$\Delta\sigma_{c,\pi/3}$(for 4|4P-like boundary at 60°, GPa)	$\Delta\sigma_{c,\pi/3}$(for vacancy line at 60°, GPa)	$\Delta\sigma_{c,0}$(for 4|4P-like boundary at 60°, GPa)	$\Delta\sigma_{c,0}$(for vacancy line at 60°, GPa)
Value	13.43	0.87	0.13	0.02	21.41	−4.85	10.23	0

TABLE 2

Crack kinking angle calculation.

Criteria	Pristine	iMo	lSe
Critical angle computed from Equation (1b)	0°	−58°	60°
Equation (1a)	Satisfied	Satisfied	Satisfied
Stability based on Inequality (1c)	Stable	Stable	Stable

any zigzag direction, this zone can be idealized as a circle whose diameter represents the characteristic size c_f.

In this study, we used the size effect method [50] for such a purpose as this method was shown to efficiently give an averaged estimation of a zone enclosing all of the inelastic deformation for quasi-brittle [50–51] and ductile materials [52]. The size effect method was constructed based on the energy contribution of an elastic zone whose size grows proportionally with the structure size and a fixed-size FPZ. The method was also shown to work best with a set of geometrically scaled structures in which the contribution of the FPZ decreased as the structure size grew., The size effect equation can be written as:

$$\sigma_N = \frac{\sigma_0}{\sqrt{1 + \frac{D}{D_0}}} \tag{4}$$

where $\sigma_N = P/tD$ is the nominal structure strength, t is the monolayer thickness, D is the relevant structure size, and P is the maximum reaction resulting from the prescribed displacement. In Eq. (4), there exist two asymptotes in the log–log scale, one of which is constant and represents the deterministic cohesive strength of the material, σ_0, and another represents the case where the elastic volume occupies the entire structure [33]. Therefore, the nominal strength would decrease as a square-root function of size. The parameters σ_0 and D_0 in Equation (4) are obtained based on the least-square fitting of the σ_N-D curves.

Fig. 7 depicts MD results obtained with geometrically scaled monolayers, for pristine, lSe, and iMo, as well as model fits using Eqs. (4) and (10) (see methods). Inspection of the plots reveal that the fracture energy values, measured by this method, are similar to those measured by the critical J-integral, as confirmed by Nguyen et al. [53] and Dönmez et al. [52]. We also note that the cohesive strength of the structure with 4|4P-like boundaries is the highest, consistent with the strengthening effect owing to the increasing bond coordination number. On the contrary, the Se-vacancy line, lSe, exhibits the lowest strength, due to the missing Mo-Se bonds on one selenium layer (Fig. 7a). However, the process zone size, c_f, of lSe is the largest and comparable to the length of the deflected distance. The guiding capability of vacancy lines and their lower cohesive strength, which allows for a gradual release of the bond energy, promotes atoms within the vacancy lines to get involved in the inelastic zone. The slip-line

boundary, iMo, on the other hand, slightly deflected the crack path, yet the release of energy becomes more pronounced with fewer atoms involved. This limits the growth of the FPZ size, yet such a size is larger than the one for the pristine material. According to Bažant et al. [50], one can choose D_0, or $3c_f$ as the target zone size. Note that, this size can increase when considering the effect of a blunt notch on the fracture energy. However, such a change can easily be accounted for by scaling c_f in accordance with G_f, which in turn can be written as a function of the notch radius [54] and the true fracture energy in a sharp-notched specimen, G_{f0}.

In silico vacancy engineering for toughening

Vacancies, as inferred from the previous sections, can alter the fracture behavior of pristine MoSe$_2$. Therefore, a design problem can be formulated consisting in the optimization of the fracture property of 2H-TMDs through the design of spatially distributed vacancies. Here, we do not aim to solve a complete optimizing problem as it would require a rigorous uncertainty quantification framework. Instead, this section introduces a few design possibilities that employ the findings previously discussed to attain tougher monolayers. Specifically, we explore spatially designed patterns such as equilateral triangle tessellation with vacancies located at all vertices. For iMo, we examined how the distance between vacancies promotes the formation of the slip-line boundary (see Fig. 8a). For lSe, we evaluated the efficiency of vacancy lines in deflecting the crack path along a desired direction using both a regular triangular pattern and a random pattern (see Fig. 8b-c).

When the iMo vacancies are spatially ordered, the crack is blunted by vacancy rows in front of the crack (Fig. 8d). Furthermore, vacancies, located on an extended line with ±60° inclination, trigger formation of a slip-line boundary (4|4P-like boundary) and enhance the fracture energy. When the distance between vacancies, l_0, is smaller than $3c_f$, the strengthening effect appears regardless of the crack location. However, when the distance between the vacancies becomes too small, the stress in the crack propagation direction is amplified and the crack tends to exhibit straight propagation (see Fig. 8e). Therefore, when considering only the maximization of J_c, there already
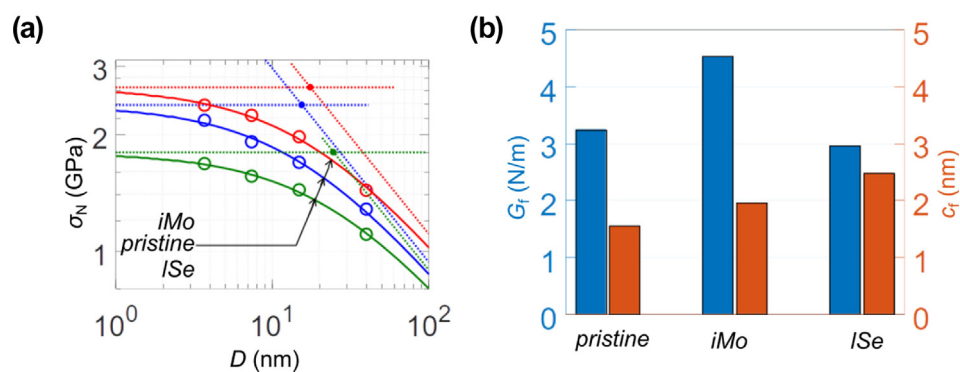
FIG. 7

(a) Size effect method fitting of MD results obtained with geometrically scaled monolayers and (b) the variation of G_f and c_f with respect to the type of vacancy.
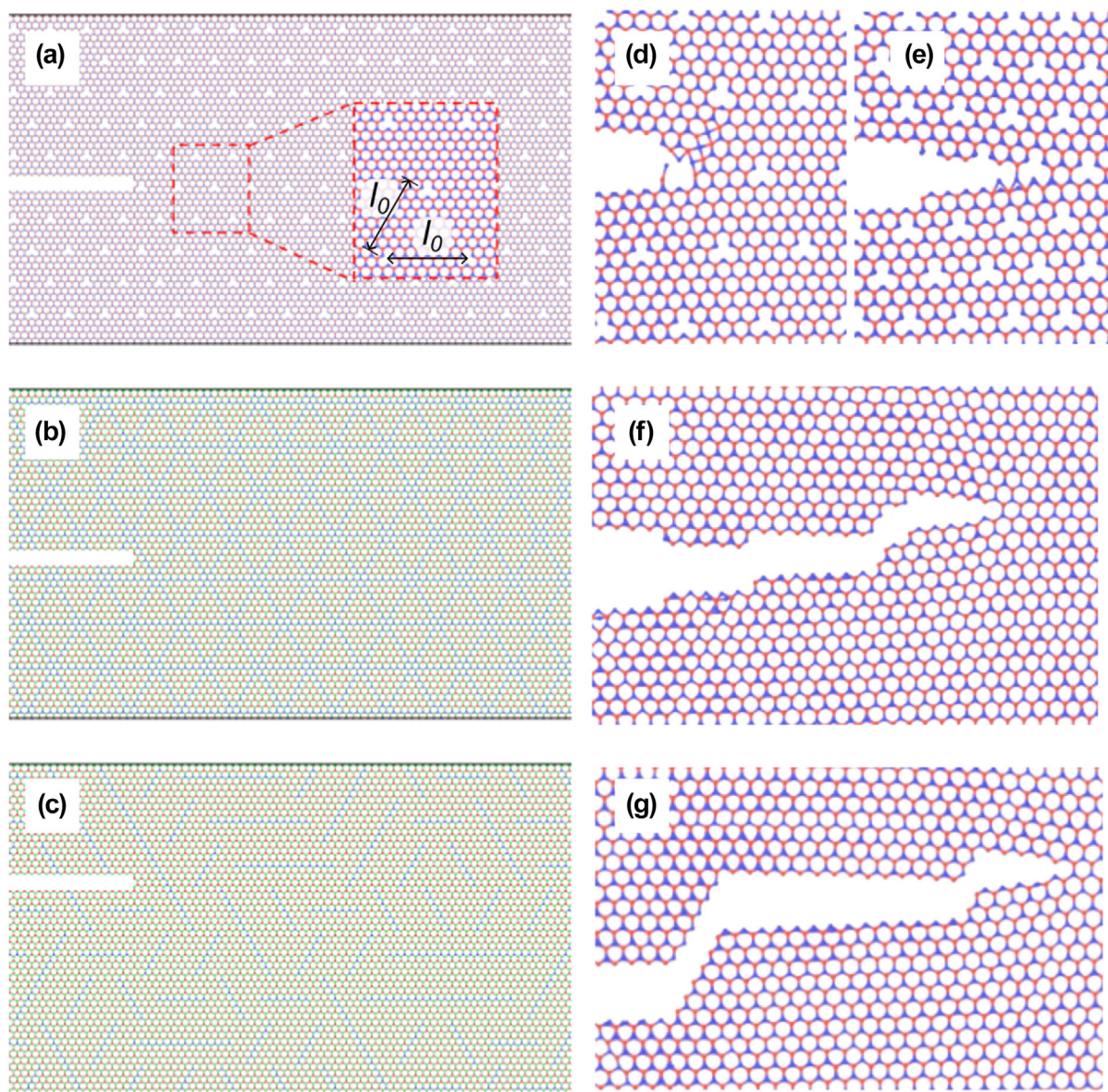

FIG. 8

Vacancy patterns (a-c) that can either allow 4|4P-like boundaries to emerge or deflect the crack path regardless of the crack location (d-g).

exist an optimum vacancy distance (density) triggering the emergence of 4|4P-like boundaries.

For the case of *lSe*, the MD simulation predicts that an ordered pattern (Fig. 8b and f) exhibits mild crack deflection (toughening), scaling with the characteristic size of the pattern. A more pronounced deflection takes place when the line of Se vacancies is random (Fig. 8c and g). This is due to the interplay between strong and weak phases (pristine versus Se-vacancy line) on the same $MoSe_2$ monolayer.

Concluding remarks

Defect engineering, e.g., through vacancies, is an active field of research because it can modify the response of 2D materials for a particular purpose. In this investigation of fracture properties, using $MoSe_2$ as an example, we show that while some types of vacancies increase resistance to crack extension, other types reduce or have virtually no effect in toughening. Using a rigorously parametrized and validated force field, we numerically investigated isolated Se vacancies (*iSe*), isolated Mo/Se_2 vacancies (*iMo/iSe$_2$*), and Se vacancy lines (*lSe*) with random configurations. Areal densities achievable in HRTEM electron radiation experiments with dosage control were employed. The study reveals that all vacancy types, except for isolated Se vacancies, *iSe*, produce crack deflections at a relatively low density. While *iMo/iSe$_2$* vacancies repel cracks, *lSe* attract and guide the crack path leading to the largest crack deflection mechanism. Interestingly, *lSe* vacancies offer the most gradual release of energy, which could provide flexibility in terms of post-peak stress deformability. However, it is the presence of *iMo* or *iSe$_2$* that produce the largest toughening mechanism by trapping the crack and blunting the tip. These results illustrate that, as previously shown in graphene [55], the presence of defects could impact the mechanical properties of 2H-TMDs by increasing their resistance to crack propagation or by extending the post-peak deformation.

We also investigated the effect of ordered *iMo* and *lSe* vacancies and found that *iMo* vacancies, =with a characteristic spacing l_0, trigger the emergence of 4|4P-like boundaries and associated toughness enhancements. On the contrary, randomly oriented *lSe* vacancies, arranged in a triangular lattice pattern, induce more crack deflection than orderly oriented *lSe* vacancies of the same areal density. It is worth noting that controlled generation of ordered vacancies, following specifically designed patterns, is currently challenging. Fortunately, a path forward is emerging from several efforts addressing this challenge [56,57]. For example, Wang et al. [30] showed that using ion beam lithography, the selective creation of S and MoS_6 vacancies could be achieved, yet the exact positioning of vacancies remains difficult. In addition, ion-assisted CVD [58,59] and epitaxial growth, based on either van der Waals interactions with crystalline substrate, or molecular beam epitaxy [60] exhibits a higher level of vacancy order. Notably, the primary knock-on space theory [61] seems to be one of the most promising tools for the precise atomic engineering of vacancies using electron irradiation. Other state-of-the-art techniques for materializing ordered patterns can be found in recent reviews [62,63]. Another remaining challenge that also requires attention is the use of defect engineering for

toughening without significantly affecting other properties (e.g., electrical or thermal conductivity).

In closing, we envision that the methodology and findings here reported will guide and advance attempts in engineering the properties of 2H-TMDs and other 2D materials. In particular, the framework introduced here will assist the design of fracture experiments with controlled vacancy type, density, and pattern. Even though we have not explored the effect of defects on other properties, such as the optoelectrical properties of $MoSe_2$ monolayers, we anticipate that the methodology and knowledge acquired in this study can be incorporated into a synergistic optimization of electrical-optical properties.

Methods

Materials and instrumentation

MoO_3 and Se powders were used as precursors in the chemical vapor deposition and placed at the center of a tube furnace. A SiO_2/Si wafer was used as the substrate and placed on top of the MoO_3 powders. The growth was conducted at 750 °C for 15 min with H_2/Ar (15% H_2) as the carrier gas.

We used atomic force microscopy (AFM) with tapping mode to characterize the thickness of $MoSe_2$ flake (Park XE-120 AFM system, South Korea). Bruker TESPA-V2 probe was used to scan a region of 5×5 μm^2 with a rate of 0.2–0.5 Hz. A 2.5:1 ratio was employed between proportional and integral grains, respectively.

The flake was transferred from the growth substrate to a SiO_2/Si substrate using the PDMS-based Dry Stamping was developed by Dong et al. [31]. A schematic of the transfer method can be found in the referenced study. The flakes were stamped onto the holey Si_3N_4 TEM grids (Ted Pella PELCO) TEM grid at 70°C, and polymer residues were washed off after that. No obvious evidence of residues was found on the transferred flake, and its height corresponded to that of a monolayer $MoSe_2$ flake, which was further confirmed by its Raman spectrum (see SI-Fig. S8).

HRTEM characterization of synthesized monolayers

HRTEM was conducted with the Argonne Chromatic Aberration-corrected TEM (ACAT, a FEI Titan 80–300 ST with an image corrector of both spherical and chromatic aberrations) at an acceleration voltage of 80 kV. Prior to imaging, the specimen was heated in a vacuum below 10^{-7} torr at 130 °C for 2 h to reduce hydrocarbon [31]. The images were taken with spherical and chromatic aberration corrected such that $Cs < 5$ μm, and $Cc < 5$ mm. Images were acquired at a controlled dose rate and total dose to mitigate vacancy formation. Hence, they reflected the high quality of the as-synthesize $MoSe_2$ flakes.

In relation to the reported vacancy analysis from HRTEM images, we note that when the defocusing Δf is close to zero, the obtained HRTEM images are amplitude contrast dominant [64], instead of phase-contrast dominant as in conventional spherical-aberration corrected HRTEM imaging. Most importantly, as shown in Fig. S11 and S12, the simulated HRTEM images (by MacTempas software) exhibit a one-to-one correspondence to the atomic models, similar to HAADF imaging.

Ab initio calculations

The training data were generated based on a density functional theory code-SIESTA version 4.0.2. [65], which was shown to be an efficient method to optimize the electronic structure and ab initio molecular dynamics simulations of molecules and solids. Depending on the type of data, either non-spin- or spin-polarized was used with the generalized gradient approximation (GGA) in the Perdew-Burke-Ernzerhof (PBE) form [66]. We chose the split polarized valence double-zeta (DZP) basis set due to the trade-off between accuracy and computational expenses [67]. Note that, SIESTA projects the electron wavefunctions and density onto a real-space grid and utilizes the non-relativistic norm-conserving Troullier-Martins pseudopotentials [68]. Intermolecular van der Waals interactions were captured by the second generation of dispersion correction (DFT-D2) as described in [69]. We performed an energy convergence test and selected a value of 250 meV for mesh cutoff and 300 Ry ($\sim$4081 eV) for energy shift. The interactions between monolayers were inhibited by a 20 Å vacuum layer. Theoretically, this should not cause any difference, but in the real-space projection, the vacuum layer size can burden and significantly decelerate the calculation time. A monolayer thickness of 7.726 Å was used to calculate per-area quantities (e.g., monolayer stresses) [82]. In the energetic and geometric optimizations, we applied no atomic constraints and optimized the structures until the forces acting on the atoms became lower than 0.01 eV-Å^{-1}. However, in the solid deforming or bond dissociation calculations, constraints were put on the box or on the atoms in the dissociated pair. To achieve accurate electronic structure calculations, we allowed a 15-Å cutoff for the set of k-points in the first Brillouin zone. However, Moreno and Soler [70] showed that the resultant k-grids would be chosen in an optimal way, based on a method utilizing an effective supercell close to the spherical shape. This approach can thus minimize the number of k-points for a given precision. The self-consistent and the conjugate gradient minimization schemes were employed for the electronic-structure calculation and for the geometry optimization, respectively.

Cohesive energies, surfaces (edges) and vacancy formation energies, and stress components were calculated with the same method as reported in our previous study [82]. Forces, however, were sampled at the atoms in selected pairs, which bonds broke first when Se and Mo molecules were annealed at a high temperature. This selection implied proximity to a realistic potential energy surface where the atoms hopped over the lowest energy barrier.

Molecular dynamics (MD) simulations

The Large-scale Atomic/Molecular Massively Parallel Simulator, or LAMMPS [71], was used for all of the atomistic simulations mentioned above. To compare MD simulations with ab initio calculations, we used the same atomic systems for most objectives except for the lattice structures and cohesive energies, in which we enlarged the size of the system for better sampling. For energy landscapes (equation of states, bond dissociation, phase transition, and dissociation of Se clusters), single-point calculations were performed on the equilibrated structures without energy minimization. For the remaining objectives, an energy minimization step was carried out with the conjugate gradient algo-

rithm (energy tolerance 0 eV, force tolerance 10^{-10} eV-Å^{-1}) before calculating the energies. For simulations with MD steps, a time step of 1 fs was used. In the fracture simulations, a monolayer MoSe$_2$ flake of a chosen domain size was first optimized and equilibrated with an NPT ensemble for 0.1 ns and then deformed at a strain rate 10^8/s. However, when crack was about to propagate, we set the rate to be 5×10^6/s. Atomic visualizations were created with OVITO. [72].

To capture the fracture response of MoSe$_2$ monolayers, while retaining important characteristics, such as out-of-plane lattice vibrations, we allowed for an out-of-plane deformation of the monolayer whose roughness wavelength is consistent with a suspended membrane geometry. We adopted a roughness quantified by Varghese et al., [73] and implemented it by placing repulsive walls above and below the monolayer at 10 Å away from their basal plane. The spacing ensured the wrinkling of the monolayers, given the dimensions, attained the desired roughness.

Potential optimization framework

We obtained the Tersoff potential parameters for this work using an updated version of the optimizing scheme presented by Zhang et al. [82]. Overall parameterization includes a few iterations, each of which comprises three steps: training, screening, and evaluating. The potential was first optimized against ab-initio data with a multi-objective genetic algorithm (NSGA-III) for a selected group of properties in the training step. Next, the optimized parameters were screened with properties that might benefit the target phenomena, i.e., fracture energy and bond-dissociation energetics. In this version, we introduced a local optimizing algorithm (Bound Optimization BY Quadratic Approximation, or BOBYQA [74]) during the screening step to encourage the convergence to the real optima. The combined global–local optimizing scheme was shown to be effective for complex potentials such as ReaxFF [75]. This effectiveness is achieved because the framework strikes the balance between a genetic algorithm that is good at escaping the local optima to find the global minimum but is bad at coming close to this optimal point. The local optimizer helps guide the individuals selected by the genetic step to their corresponding extrema. At the end of this step, we prescribed a combination of maximum percentage errors to identify promising candidates, in which a smaller percentage was given to the criterion that is directly related to the fracture behavior, e.g., bond dissociating energy and force, surface energy, and phase transformation energy landscape. In the evaluating step, we tested the performance of a few selected sets of parameters on fracture-related behaviors of structures that had the size of two to ten nanometers and compared them to experimental results (or large-scale first-principle results if available). If such validations were absent, a few properties that were physically correlated to fracture were evaluated instead. Also, an optional test for transferability could also be performed to evaluate the capability of the potential in other scenarios. After each iteration, we evaluated the relation of the involved properties using a normalized covariance matrix and principal component analysis. This served to guide the selection of training and screening properties for the next iteration, which might

include regrouping, adding, and eliminating some properties to better optimize the target behaviors.

Following the previous study, we chose a population size of 168 individuals [76]. Ten replicas with different randomly generated seeds were created, each of which was run for 500 generations. This number of generations was shown to be adequate for the NSGA-III to converge [82]. For crossover, a simulated binary operator was used with a crossover probability of 1 and a crowding degree η of 30. For mutation, we used a polynomial operation with a mutation probability of 1 and η of 20. The statistics of each replica were output after a number of generations (20 in this study) to monitor the optimization progress. At the end, we combined the optimized parameters from all replicas for the local optimization process and the screening step. We used Python (3.7.7) and the Distributed Evolutionary Algorithms in Python (DEAP) package to run the genetic algorithm [77]. The local optimizer was, however, implemented based on the Python Parallel Global Multiobjective Optimizer [78] (PyGMO) package. SCOOP (0.7.1.1) [79] was used to distribute the tasks for parallel computing. The optimization time scaled with the complexity of a selected potential.

Atomistic-to-continuum mapping of the mechanical fields and J-integral as a measure of fracture resistance

The quantification of J-integral requires a technique to map the discrete quantities into continuum fields, and such a procedure is convenient as per-atom stresses and energy density can be easily output from LAMMPS. In this study, we used an atomistic-to-continuum mapping scheme developed by Jones and Zimmerman [80]. Each per-atom quantities would be evaluated based on a kernel function that satisfies the following requirements:

$$\psi > 0; \int_{\Omega} \psi dV = 1 \tag{5}$$

For 2D materials, we employed a cylindrical kernel instead of a spherical one. The z-thickness of the cylinder was equal to the interlayer distance between monolayers (7.726 Å). This quantity, however, only served to ensure the consistency between stress components in a monolayer and their 3D counterparts. The function ψ is written as:

$$\psi = \frac{20}{6\pi R_c^2 t} \left[1 - 3\left(\frac{r}{R_c}\right)^2 + 2\left(\frac{r}{R_c}\right)^3 \right] \tag{6}$$

where R_c is the averaging radius and t is the monolayer thickness. Note that, strain components were calculated from the displacement field, and they should be estimated at the same spatial position as the stress components in the J-integral formulation. The grid points to map the displacement field (and the q-field) were therefore different from the ones used to map the stress–strain fields. We borrowed a concept from the finite element method (FEM) and placed the displacement-field grid points at the nodes of triangulation generated by a Python discretization package (meshzoo) and the stress-field grid points located at the quadrature point associated with each triangle. The use of FE shape functions also facilitated the calculation of derivative terms [81].

A continuum quantity was then calculated from:

$$W(X,t) = \sum_{\alpha} \left(\phi^{\alpha}(t) - \phi_X^{\alpha} \right) \psi(X - X^{\alpha}) \tag{7}$$

where α was the total number of atoms in the averaging horizon. ϕ could represent displacement components, stress components, energy density or q-value and W was the corresponding continuum quantity.

The field value at a position different from the grid points can be interpolated using shape functions $\mathbf{N}$ and their gradients:

$$u(X,t) = \sum_i N_i(X,t)u_i; \nabla u(X,t) = \sum_i \nabla N_i(X,t)u_i \tag{8}$$

where N_i's are the shape functions and u_i are the field values at vertex i.

The stress terms are extracted from interatomic interactions by [71]:

$$
\begin{aligned}
\sigma_{ab} = &\frac{1}{2}\sum_{n=1}^{N_p}\left(r_{1_a}F_{1_b} + r_{2_a}F_{2_b}\right) + \frac{1}{2}\sum_{n=1}^{N_b}\left(r_{1_a}F_{1_b} + r_{2_a}F_{2_b}\right) \\
&+ \frac{1}{3}\sum_{n=1}^{N_a}\left(r_{1_a}F_{1_b} + r_{2_a}F_{2_b} + r_{3_a}F_{3_b}\right) \\
&+ \frac{1}{4}\sum_{n=1}^{N_d}\left(r_{1_a}F_{1_b} + r_{2_a}F_{2_b} + r_{3_a}F_{3_b} + r_{4_a}F_{4_b}\right) \\
&+ \frac{1}{4}\sum_{n=1}^{N_i}\left(r_{1_a}F_{1_b} + r_{2_a}F_{2_b} + r_{3_a}F_{3_b} + r_{4_a}F_{4_b}\right) + \sum_{n=1}^{N_f} r_{i_a}F_{i_b}
\end{aligned} \tag{9}
$$

To alleviate the noise from thermal oscillation, we performed the mapping on the time-averaged snapshot of the simulations. Each snapshot was therefore an average of 1000 frames.

Estimate of process zone size from size effect theory

The fracture energy G_f and the characteristic size of the FPZ, c_f, can then be computed from σ_0 and D_0 using the following relations:

$$G_f = \sigma_0^2 g(\alpha_0) D_0 / E, c_f = g(\alpha_0) D_0 / g'(\alpha_0) \tag{10}$$

where $g(a/D)$ and $g'(a/D)$ are the dimensionless energy release rate and its derivative, respectively, with $\alpha = a/D$, as the independent variable. These functions can be found in Bazant et al. [33].

Data availability

Data will be made available on request.

Declaration of competing interest

The authors declare that they have no known competing financial interests or personal relationships that could have appeared to influence the work reported in this paper.

Acknowledgements

Appendix A. Supplementary Material

Supplementary data to this article can be found online at https://doi.org/10.1016/j.mattod.2023.10.002.

References

[1] R.G. Dickinson, L. Pauling, J. Am. Chem. Soc. 45 (6) (1923) 1466.
[2] S. Manzeli et al., Nat. Rev. Mater. 2 (8) (2017) 1.
[3] B. Radisavljevic et al., Nat. Nanotechnol. 6 (3) (2011) 147.
[4] O. Lopez-Sanchez et al., Nat. Nanotechnol. 8 (7) (2013) 497.
[5] J. Reyes-Retana, F. Cervantes-Sodi, Sci. Rep. 6 (1) (2016) 1.
[6] S.S.P. Nathamgari et al., Nano Lett. 19 (6) (2019) 4052.
[7] T.H. Choudhury et al., Annu. Rev. Mat. Res. 50 (2020) 155.
[8] D.L. Keshebo et al., J. Membr. Sci. 634 (2021) 119419.
[9] X. Zhang et al., Small (2022) 2105194.
[10] T.H. Ly et al., Nat. Commun. 8 (1) (2017) 1.
[11] Q.D. Truong et al., RSC Adv. 8 (58) (2018) 33391.
[12] J. Lin et al., ACS Nano 9 (5) (2015) 5189.
[13] C. Wei et al., ACS Appl. Mater. Interfaces 11 (28) (2019) 25264.
[14] I.M. Ifti et al., Effect of Vacancy on Electronic Properties of MX 2 (M= Mo, W and X= S, Se) Monolayers, in: 2020 11th International Conference on Electrical and Computer Engineering (ICECE), IEEE, 2020, p. 391.
[15] S.M. Hus, A.-P. Li, Prog. Surf. Sci. 92 (3) (2017) 176.
[16] H.-P. Komsa et al., Phys. Rev. Lett. 109 (3) (2012) 035503.
[17] Y. Yang et al., Adv. Mater. 29 (2) (2017) 1604201.
[18] I. Benedetti et al., J. Mech. Phys. Solids 112 (2018) 66.
[19] T. Cui et al., Nat. Mater. 19 (4) (2020) 405.
[20] Q. Tang, J. Mater. Chem. C 6 (35) (2018) 9561.
[21] Q. Chen et al., ACS Nano 12 (8) (2018) 7721.
[22] J. Chen et al., Nano Lett. 22 (8) (2022) 3289.
[23] A.W. Robertson et al., ACS Nano 7 (5) (2013) 4495.
[24] S. Wang et al., ACS Nano 10 (11) (2016) 9831.
[25] A. Falin et al., ACS Nano 15 (2) (2021) 2600.
[26] A. Mahata et al., Nano-Struct. Nano-Objects 18 (2019) 100247.
[27] H. Bao et al., Nano Express 2 (4) (2021) 040006.
[28] H. Huang et al., Nanoscale 12 (3) (2020) 1247.
[29] X. Zhang et al., Proc. Natl. Acad. Sci. 119 (45) (2022).
[30] G. Wang et al., Adv. Sci. 9 (22) (2022) 2200700.
[31] S. Dong et al., Mater. Today 52 (2022) 31.
[32] J.R. Rice, G.F. Rosengren, J. Mech. Phys. Solids 16 (1) (1968) 1.
[33] Z.P. Bazant, J. Planas, Fracture and Size Effect in Concrete and other Quasibrittle Materials, CRC Press, 1997.
[34] Z.P. Bažant, L. Cedolin (2010).
[35] M. Parrinello, A. Rahman, J. Appl. Phys. 52 (12) (1981) 7182.
[36] J. Hutchinson, J. Mech. Phys. Solids 16 (1) (1968) 13.
[37] A. Yoshimura et al., Nanoscale (2023).
[38] J. Jiang et al., Research (2019) 2019.
[39] K. Wu et al., Nano Res. 11 (8) (2018) 4123.
[40] G. Henkelman, H. Jónsson, J. Chem. Phys. 113 (22) (2000) 9978.
[41] G. Henkelman et al., J. Chem. Phys. 113 (22) (2000) 9901.
[42] F. Erdogan, G. Sih (1963).
[43] R. Nuismer, Int. J. Fract. 11 (2) (1975) 245.
[44] G.C. Sih, Int. J. Fract. 10 (3) (1974) 305.
[45] M. Amestoy et al., Adv. Fracture Res.(Fracture 81) 1 (1981) 107.
[46] H. Richard, Inderscience Enterprises Ltd., Genf, 1987.
[47] H. Richard et al., Fatigue Fract. Eng. Mater. Struct. 28 (1–2) (2005) 3.
[48] M. Romanowicz, Eng. Fract. Mech. 214 (2019) 544.
[49] S. Zhou, S. Guo, Int. J. Rock Mech. Min. Sci. 46 (8) (2009) 1389.
[50] Z.P. Bažant, M.T. Kazemi, J. Am. Ceram. Soc. 73 (7) (1990) 1841.
[51] H.T. Nguyen et al., J. Appl. Mech. 87 (7) (2020) 071012.
[52] A.A. Dönmez et al., J. Mech. Phys. Solids 173 (2023) 105222.
[53] H.T. Nguyen et al., Extreme Mech. Lett. 43 (2021) 101141.
[54] T. Nishida et al., J. Am. Ceram. Soc. 77 (2) (1994) 606.
[55] T. Zhang et al., J. Mech. Phys. Solids 67 (2014) 2.
[56] H.-P. Komsa et al., Phys. Rev. B 88 (3) (2013) 035301.
[57] H. Park et al., Small 17 (23) (2021) 2100693.
[58] H.G. Ji et al., Chem. Mater. 30 (2) (2018) 403.
[59] W. Zhou et al., Nano Lett. 13 (6) (2013) 2615.
[60] X. He et al., Nat. Commun. 10 (1) (2019) 1.
[61] C. Su et al., Sci. Adv. 5 (5) (2019) eaav2252.
[62] M. Cavallini, D. Gentili, ChemPlusChem 87 (3) (2022) e202100562.
[63] Z. Hu et al., Chem. Soc. Rev. 47 (9) (2018) 3100.
[64] H. Wang et al., Phys. Rev. X 6 (1) (2016) 011027.
[65] J.M. Soler et al., J. Phys. Condens. Matter 14 (11) (2002) 2745.
[66] J.P. Perdew et al., Phys. Rev. Lett. 77 (18) (1996) 3865.
[67] T.H. Dunning, P.J. Hay, Modern Theoret. Chem. 3 (1977) 1.
[68] N. Troullier, J.L. Martins, Phys. Rev. B 43 (3) (1991) 1993.
[69] S. Grimme, J. Comput. Chem. 27 (15) (2006) 1787.
[70] J. Moreno, J.M. Soler, Phys. Rev. B 45 (24) (1992) 13891.
[71] A.P. Thompson et al., Comput. Phys. Commun. (2021) 108171.
[72] A. Stukowski, Model. Simul. Mater. Sci. Eng. 18 (1) (2009) 015012.
[73] A. Varghese et al., Nanoscale 9 (11) (2017) 3818.
[74] M.J. Powell, Cambridge NA Report NA2009/06, University of Cambridge, Cambridge, 2009, p. 26.
[75] G. Shchygol et al., J. Chem. Theory Comput. 15 (12) (2019) 6799.
[76] K. Deb, H. Jain, IEEE Trans. Evol. Comput. 18 (4) (2013) 577.
[77] F.-A. Fortin et al., J. Machine Learn. Res. 13 (1) (2012) 2171.
[78] F. Biscani, D. Izzo, J. Open Source Softw. 5 (53) (2020) 2338.
[79] Y. Hold-Geoffroy, et al., Once you SCOOP, no need to fork. In: Proceedings of the 2014 Annual Conference on Extreme Science and Engineering Discovery Environment, 2014, pp. 1.
[80] R.E. Jones, J.A. Zimmerman, J. Mech. Phys. Solids 58 (9) (2010) 1318.
[81] F. Jacob, B. Ted, A First Course in Finite Elements, Wiley, 2007.
[82] Xu Zhang et al., Multi-objective parametrization of interatomic potentials for large deformation pathways and fracture of two-dimensional materials, npj Computational Materials (7.1) (2021) 113.